

Simulating Cosmic Reionization at Large Scales II: the 21-cm Emission Features and Statistical Signals

Garrelt Mellema^{1,2*}, Ilian T. Iliev³, Ue-Li Pen³, Paul R. Shapiro⁴

¹ ASTRON, P.O. Box 1, NL-7990 AA Dwingeloo, The Netherlands

² Sterrewacht Leiden, P.O. Box 9513, NL-2300 RA Leiden, The Netherlands

³ Canadian Institute for Theoretical Astrophysics, University of Toronto, 60 St. George Street, Toronto, ON M5S 3H8, Canada

⁴ Department of Astronomy, University of Texas, Austin, TX 78712-1083

2 December 2024

ABSTRACT

We present detailed predictions for the redshifted 21cm signal from the epoch of reionization. These predictions are obtained from radiative transfer calculations on the results of large scale (100/h Mpc), high dynamic range, cosmological simulations. We consider several scenarios for the reionization history, of both early and extended reionization. From the simulations we construct and analyze a range of observational characteristics, from the global signal, via detailed images and spectra, to statistical representations of rms fluctuations, angular power spectra, and probability distribution functions to characterize the non-gaussianity of the 21cm signal. We find that the different reionization scenarios produce quite similar observational signatures, mostly differing in the redshifts of 50% reionization, and of final overlap. All scenarios show a gradual transition in the global signatures of mean signal and rms fluctuations, which would make these more difficult to observe. Individual features such as deep gaps and bright peaks are substantially different from the mean and mapping these with several arcminutes and 100s of kHz resolution would provide a direct measurement of the underlying density field and the geometry of the cosmological HII regions, although significantly modified by peculiar velocity distortions. The presence of late emission peaks suggest these to be a useful target for observations. The power spectra during reionization are strongly boosted compared to the underlying density fluctuations. The strongest statistical signal is found around the time of 50% reionization and displays a clear maximum at an angular scale of $\ell \sim 3000-5000$. We find the distribution function of emission features to be strongly non-gaussian, with an order of magnitude higher probability of bright emission features. These results suggest that observationally it may be easier to find individual bright features than deriving the power spectra, which in its turn is easier than observing individual images.

Key words: cosmology: theory — diffuse radiation — intergalactic medium — large-scale structure of universe — galaxies: formation — radio lines: galaxies

1 INTRODUCTION

Observations of the redshifted 21-cm line of hydrogen are currently emerging as the most promising approach for direct detection of the epoch of reionization, and possibly of the preceding period before the formation of the first ionizing sources, the Cosmic Dark Ages. Several large radio interferometer arrays are currently either operational, under construction or being planned that have the potential to detect this redshifted 21-cm emission. These projects include PAST¹ (already operating in north-western China), GMRT² (oper-

ating in India), LOFAR³ (under construction in the Netherlands), MWA⁴ (to be located in Western Australia), and SKA⁵.

The observations will be complicated due to the combined effects of (in order of increasing distance from us) possible radio frequency interference from terrestrial emitters (in particular in the 87-108 MHz FM band), ionospheric fluctuations, the galactic foreground, and unresolved intergalactic radio sources, all of which are much stronger than the expected redshifted 21-cm signal. Therefore it is crucial to understand the characteristics of the reionization 21-cm signal in some detail. This can help both in planning of the experiments, so that they are optimized for the expected signal,

* e-mail: gmellema@astron.nl

¹ <http://web.phys.cmu.edu/~past/>

² <http://www.ncra.tifr.res.in>

³ <http://www.lofar.org>

⁴ <http://web.haystack.mit.edu/arrays/MWA>

⁵ <http://www.skatelescope.org>

and once data is available, can direct us in separating the strong foregrounds and interpreting the signal correctly. Predicting the unique signatures of reionization is quite hard. The Λ CDM framework for cosmological structure formation is now well-established, the fundamental cosmological parameters are increasingly better constrained, and the basic physical processes during reionization are fairly well-understood. However, we will be probing redshifts for which little or no observational data is currently available, and many of the relevant parameters are at best poorly constrained. For example, a number of choices remain open regarding the nature of the ionizing sources during reionization, their numbers, photon production efficiencies and spectra.

Another complication is the large dynamic range required from any simulation which aims to predict the redshifted 21-cm emission. Within the hierarchical structure formation paradigm the ionizing photon emissivity during reionization is dominated by numerous dwarf-size galaxies, rather than by larger ones, which at high redshifts are too rare to make an appreciable contribution. On the other hand, the strong source clustering at high redshifts means that ionized bubbles quickly overlap locally and each H II region typically contains a large number of sources. This leads to the formation of large ionized regions, of size tens of comoving Mpc or more, which requires simulation volumes of size ~ 100 Mpc for proper treatment. Cosmological simulations resolving dwarf galaxies in such large volumes are only now becoming possible. Even more difficult and computationally-intensive is the transfer of ionizing radiation from the tens of thousands up to millions of individual galaxies found in such a large volume.

To date there have been only a few cosmological simulations which studied the redshifted 21-cm. Most of these resolved this difficulty by considering small enough regions (thus achieving the high resolution required) either during the Cosmic Dark Ages (Shapiro et al. 2005; Kuhlen et al. 2006) or during reionization (Carilli et al. 2002; Ciardi & Madau 2003; Gnedin & Shaver 2004; Furlanetto et al. 2004; Valdes et al. 2006). An alternative approach proposed recently is to simulate large regions at low resolution and thus without resolving individual small sources, and to include their effect in an averaged, approximate way (Kohler et al. 2005).

Recently we presented the first N-body and radiative transfer simulations which considered a sufficiently large volume, at the same time resolved all dwarf galaxies in that volume and accounted for their individual contributions to reionization (Iliev et al. 2005, hereafter Paper I). We first performed an N-body simulation with 4.3 billion particles in a $(100 h^{-1} \text{ Mpc})^3$ volume. This provided us with all halos with masses above $2.5 \times 10^9 M_\odot$ and the cosmological evolution of the density field. We then imported these results into a new fast and precise radiative transfer code called C^2 -Ray (Mellema et al. 2006). In Paper I we presented our simulation methodology, as well as the results for the large-scale geometry (often also referred to as topology) of reionization, i.e. the size and number distributions of the H II regions in space, their evolution in time, and the power spectra of the resulting neutral and ionized density fields. We showed that the fluctuations in both the neutral and the ionized density are strongly boosted due to the patchiness of reionization. We also demonstrated that the probability distribution function (PDF) of the ionized fraction and the ionized density are generally strongly non-Gaussian at all scales and quantified their level of departure from non-Gaussianity for the first time. We also derived the PDF and the mean optical depths to Ly- α photons (related to the Gunn-Peterson effect in spectra of distant sources). In this paper we present detailed predictions for the redshifted 21-cm

signal, including results from several new simulations in addition to the original one from Paper I. We focus on generic predictions of the observational properties from our simulations, rather than aiming our analysis to specific radio-interferometry arrays.

The lay-out of this paper is as follows. In Sect. 2 we describe the basic procedures of extracting the 21-cm signal from the data and the assumptions that go into that. In Sect. 3 we discuss our simulations and their basic parameters and features. In Sect. 4 we present the evolution of the mean 21-cm signal and its implications. Next, in Sect. 5 we discuss how the reionization geometry would be seen at redshifted 21-cm line and the dependence of this on the adopted observational beam shape. The first 21-cm signals to be detected would quite possibly be individual, bright features. These are discussed in Sect. 6. Finally, the statistics of the 21-cm emission signal is discussed in Sect. 7. Our conclusions are summarized in Sect. 8.

Throughout this paper we use the concordance flat ($\Omega_k = 0$) Λ CDM cosmology with parameters $(\Omega_m, \Omega_\Lambda, \Omega_b, h, \sigma_8, n) = (0.27, 0.73, 0.044, 0.7, 0.9, 1)$ (Spergel et al. 2003), where Ω_m , Ω_Λ , and Ω_b are the total matter, vacuum, and baryonic densities in units of the critical density, σ_8 is the standard deviation of linear density fluctuations at present on the scale of $8h^{-1} \text{ Mpc}$, and n is the index of the primordial power spectrum of density fluctuations.

2 THE REDSHIFTED 21-CM SIGNAL

The 21-cm radio line, in either emission or absorption is due to a spin-flip transition of neutral hydrogen atoms. This transition quickly enters into equilibrium with the CMB photons and hence it needs to be decoupled from the CMB by some mechanism in order to become observable. This could occur either through collisions with other hydrogen atoms and free electrons (Purcell & Field 1956; Field 1959; Allison & Dalgarno 1969; Zygelman 2005) or through Ly- α photon pumping (Wouthuysen 1952; Field 1959; Hirata 2005; Chuzhoy & Shapiro 2005).

The differential brightness temperature with respect to the CMB of the redshifted 21-cm emission is determined by the density of neutral hydrogen, ρ_{HI} , and its spin temperature, T_s (see e.g. Morales & Hewitt 2004; Shapiro et al. 2005, for detailed discussions). It is given by

$$\delta T_b = \frac{T_s - T_{\text{CMB}}}{1 + z} (1 - e^{-\tau}) \quad (1)$$

where z is the cosmological redshift, T_{CMB} is the temperature of the CMB radiation at redshift z , and the optical depth τ is (e.g. Iliev et al. 2002):

$$\tau(z) = \frac{3\lambda_0^3 A_{10} T_* n_{\text{HI}}(z)}{32\pi T_s H(z)} = \frac{0.28}{T_s} \left(\frac{1+z}{10} \right)^{3/2} (1 + \delta) \quad (2)$$

where $\lambda_0 = 21.16 \text{ cm}$ is the rest-frame wavelength of the line, $A_{10} = 2.85 \times 10^{-15} \text{ s}^{-1}$ is the Einstein A-coefficient, $T_* = 0.068 \text{ K}$ corresponds to the energy difference between the two levels, $1 + \delta = \rho_{\text{HI}}/\langle \rho_H \rangle$ is the mean density of neutral hydrogen in units of the mean density of hydrogen at redshift z , and $H(z)$ is the redshift-dependent Hubble constant,

$$\begin{aligned} H(z) &= H_0 [\Omega_m (1+z)^3 + \Omega_k (1+z)^2 + \Omega_\Lambda]^{1/2} \\ &\approx H_0 E(z) = H_0 \Omega_m^{1/2} (1+z)^{3/2}, \end{aligned} \quad (3)$$

where H_0 is the value at the present day, and the last expression is valid for $z \gg 1$.

Assuming $\tau \ll 1$ (which is always correct for the redshifts

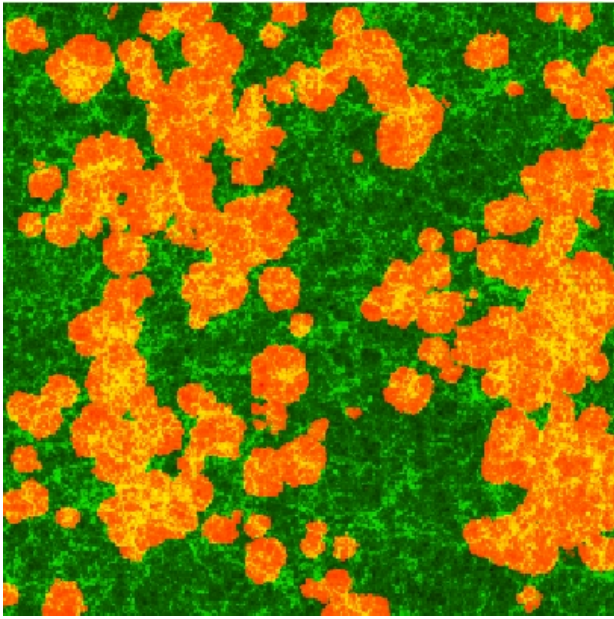


Figure 1. A cut through the simulation box of our high resolution, f2000_406 run, at $z=13.89$. The neutral gas density is shown in green. The orange overlay shows the ionized regions. Each side of the square corresponds to a comoving length of $100 h^{-1} \text{ Mpc}$.

of interest here, except for some lines of sight through mini-halos (Iliev et al. 2002), equation 1 becomes

$$\begin{aligned} \delta T_b &\approx (3.1 \text{mK}) h^{-1} \frac{(1+z)^2}{E(z)} \frac{(T_S - T_{\text{CMB}})}{T_S} (1 + \delta) \\ &\approx (27 \text{mK}) \left(\frac{1+z}{10} \right)^{1/2} \frac{(T_S - T_{\text{CMB}})}{T_S} (1 + \delta), \end{aligned} \quad (4)$$

with h being H_0 in units of $100 \text{ km s}^{-1} \text{ Mpc}^{-1}$.

To obtain an appreciable signal, the spin temperature T_S should differ significantly from T_{CMB} . The gas kinetic temperature itself is expected to be above the CMB temperature due to heating by shocks, X-rays, and Ly- α photons, thus the redshifted 21-cm is generally in emission. Decoupling through collisions is efficient only at very high- z and in significantly overdense and heated regions, mostly inside collapsed halos (Iliev et al. 2002, 2003; Shapiro et al. 2005). Once the first stars turn on, the Ly- α photons produced by them can easily pump the population to the gas kinetic temperature (e.g., Ciardi & Madau 2003). Thus, during reionization one can assume that globally $T_S \approx T_{\text{gas}} \gg T_{\text{CMB}}$. In this case the precise value of T_S becomes irrelevant, and the observable differential brightness temperature is only a function of redshift and H I density. This is the assumption we adopt throughout this paper. This should note that during the earliest stages of reionization, when sources were few and could only affect their local environments this assumption might not hold (Barkana & Loeb 2005b; Chuzhoy & Shapiro 2005), but such effects are still difficult to implement in simulations.

3 THE SIMULATIONS

The details of our methodology were described in Paper I. Here we only summarize the relevant parameters and briefly discuss the main features of each of the simulations used in the current work. Our base N-body simulation was performed using the

Table 1. Simulation parameters and global reionization history results

	f2000	f2000_406	f250	f2000C
mesh	203^3	406^3	203^3	203^3
f_γ	2000	2000	250	2000
C_{subgrid}	1	1	1	$C(z)$
$z_{50\%}$	13.6	13.5	11.7	12.6
z_{overlap}	11.3	~ 11	9.3	10.15
τ_{es}	0.145	~ 0.14	0.121	0.135

particle-mesh code PMFAST (Merz et al. 2005) and has a total of $1624^3 = 4.3$ billion particles on a 3248^3 computational mesh. The computational volume is $(100 h^{-1} \text{ Mpc})^3$. We found all halos with masses above $2.5 \times 10^9 M_\odot$ (corresponding to 100 particles or more) on a large number of density time-slices. We then imported these results into a new fast and precise radiative transfer code called C^2 -Ray which we have developed (Mellema et al. 2006). The code has been tested in detail against available analytical solutions (Mellema et al. 2006) and in comparison with other radiative transfer codes (Iliev et al. 2006). The radiative transfer runs have mesh resolutions of 203^3 and 406^3 , since the full N-body mesh, at 3248^3 , is still well beyond the current computational capabilities. Our ionizing sources correspond to all the halos found in our volume at the full resolution of the underlying N-body simulation. No artificial grouping of sources has been employed, with the exception of combining sources which happen to be inside the same radiative transfer cell, something that affects only a small fraction of the sources.

We present the results of four simulations, all of which use the same box size, density fields and halo catalogues, but each with different the sub-grid physics, as follows. Three of these simulations are run at the same 203^3 mesh resolution, but making different assumptions about the gas clumping at small scales and about the photon production efficiencies of the ionizing sources. The fourth simulation is one run at the higher mesh resolution of 406^3 , but otherwise adopting the same assumptions. All simulations and their basic parameters and features are summarized in Table 1.

Our first case, which we will call f2000 hereafter, is the simulation we presented in detail in Paper I. It assumes a source photon production efficiency (which is a combination of the total number of ionizing photons emitted by the stars per unit time, the star formation efficiency and the escape fraction) of $f_\gamma = 2000$ photons per halo atom, which corresponds to a top-heavy initial mass function (IMF). It reached overlap (defined as more than 99% ionization by mass) at a redshift of $z = 11.3$. The resulting optical depth for electron scattering is $\tau_{\text{es}} = 0.145$, within the 2σ limits of the new WMAP value, $\tau_{\text{es}} = 0.09 \pm 0.03$ (Page et al. 2006). Our second case is the same simulation as f2000 but at a higher mesh resolution of 406^3 (hereafter called f2000_406). In general the results closely match the f2000 run. The density field is resolved better and the H II regions have somewhat less spherical shapes than in the lower resolution run (as could be expected). The global evolution is slightly slower due to the better-resolved density field, resulting in higher effective gas clumping. As an illustration we show in Fig. 1 a slice

through the simulation volume of the density and ionization structures at redshift $z = 13.89$ extracted from this high-resolution run.

Our third simulation (labelled f250) adopts a lower photon production efficiency of 250 photons per halo atom, corresponding to either a slightly top-heavy IMF, or a Salpeter IMF combined with a bit higher escape fraction and star formation efficiency at these high redshifts. This simulation reached overlap at redshift $z = 9.3$. The resulting optical depth for electron scattering is $\tau_{\text{es}} = 0.121$, within the $1-\sigma$ limit of the new WMAP value.

The fourth case included in this paper, called f2000C, assumes the same source efficiency as f2000, but adds the effect of sub-grid gas inhomogeneities, described by a mean volume-averaged clumping factor, $C_{\text{subgrid}} = \langle n^2 \rangle / \langle n \rangle^2$, given by

$$C_{\text{subgrid}}(z) = 27.466e^{-0.114z+0.001328z^2}. \quad (5)$$

This fit to the small-scale clumping factor is an improved version of the one we presented in Iliev et al. (2005). To derive it we used another PMFAST simulation, with the same computational mesh, 3248^3 , and number of particles, 1624^3 , but a much smaller computational volume, $(3.5 \text{ h}^{-1} \text{ Mpc})^3$, and thus much higher resolution. These parameters correspond to particle mass of $10^3 M_{\odot}$ and minimum resolved halo mass of $10^5 M_{\odot}$. This box size was chosen so as to resolve the scales most relevant to the clumping - on smaller scales the gas would be Jeans smoothed, while on larger scales the density fluctuations are already present in our computational density fields and should not be included again. The expression in equation (5) excludes the matter residing inside collapsed halos since these contribute to the recombination rate differently from the unshielded IGM. The minihalos are self-shielded, which results in their lower contribution to the total number of recombinations than one would infer from simple gas clumping argument (Shapiro et al. 2004; Iliev et al. 2005), while the larger halos are ionizing sources and their recombinations are implicitly included in the photon production efficiency f_{γ} through their escape fraction. The f2000C case reached overlap at a redshift of 10.15. The resulting integral optical depth of electron scattering is $\tau_{\text{es}} = 0.135$. For completeness, we are also running a simulation f250C, which combines low-efficiency sources with sub-grid gas clumping, but this run is still not completed, so we have not included it in the current paper. It is expected to reach overlap at a redshift of ~ 8 .

The value for the electron scattering optical depth reported from the 3-year WMAP data, 0.09 ± 0.03 (Page et al. 2006), is substantially below the first year value (0.17 ± 0.04 , Kogut et al. 2003). Our simulation results fall roughly within the overlap region between these two results and within $2-\sigma$ from the new result. Moderate changes in the simulation parameters, e.g. assuming lower luminosity sources and/or accounting better for the small-scale gas clumping as in f2000C and f250 easily extends the reionization process until significantly later times. We expect simulation f250C to approach the new WMAP value even better.

In this paper we will use results from simulations, f2000, f2000C and f250, and results from f2000_406 only as comparison to f2000. We will not present any results from the still-running simulation f250C. A more detailed comparison of their different reionization histories and implications will be the subject of a future paper.

For reference we show in Fig. 2 the frequency of the redshifted 21-cm emission, ν_z (top), the angular size on the sky, $\Delta\theta_{\text{box}}$ (middle), and its total bandwidth, $\Delta\nu_{\text{box}}$ (bottom), versus redshift, for our $100 h^{-1} \text{ Mpc}^3$ comoving computational volume. These quan-

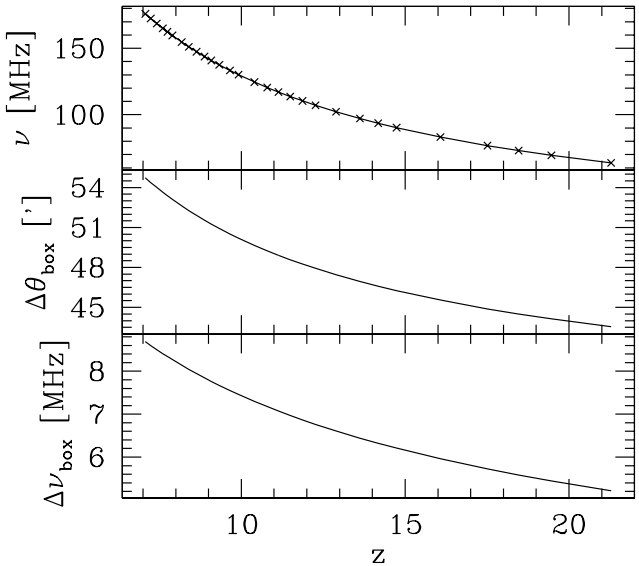


Figure 2. Simulation size and output times: (top) the frequency of the 21-cm signal (the crosses indicate the redshifts at which we have model data), (middle) the angular size on the sky of our computational volume, and (bottom) the frequency width of our computational volume, all plotted vs. redshift z .

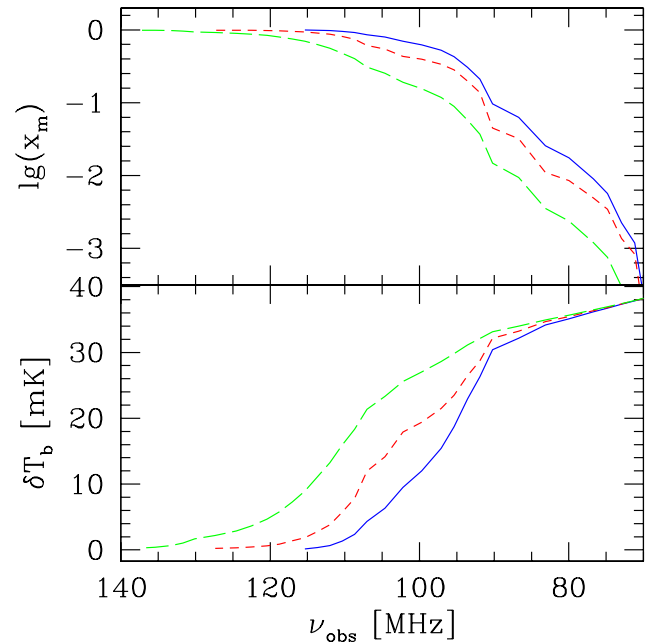


Figure 3. Evolution of (top) the mean mass ionized fraction, x_m , and (bottom) the mean differential brightness temperature, δT_b , both as a functions of frequency for f2000 (solid, blue), f2000C (short-dashed, red) and f250 (long-dashed, green).

ties are given by

$$\nu_z = \nu_0 / (1 + z) \quad (6)$$

$$\Delta\theta_{\text{box}} = \frac{L_{\text{box}}}{(1 + z)D_A(z)} \quad (7)$$

$$\Delta\nu_{\text{box}} = \frac{\nu_0 H_0 E(z) L_{\text{box}}}{c(1 + z)^2}, \quad (8)$$

where $D_A(z)$ is the angular diameter distance, $L_{\text{box}} = 100/h$ Mpc is the comoving size of our box, c is the speed of light and $\nu_0 = 1.420$ GHz is the rest-frame frequency of the line. We see that our computational box corresponds to almost one degree on the sky and a range of 5.5 to 7 MHz in frequency. The intrinsic resolution of our data is approximately 14'' (7'') in the spatial direction, and 30 kHz (15 kHz) in frequency for our 203^3 (406 3) meshes. None of the currently planned experiments will achieve similar spatial resolution. The estimates for both PAST and LOFAR are that they will have synthesized beams of $\sim 3'$. Their intrinsic frequency resolution will actually be somewhat higher than in our simulations, e.g. around 1 kHz for LOFAR. However, to obtain sufficient flux sensitivity, the data will be integrated over significantly larger bandwidths, e.g. around 200 kHz for LOFAR, which approximately corresponds to 7 (14) of our cells at 203^3 (406 3) resolution.

4 THE EVOLUTION OF THE MEAN BACKGROUND

The simplest global measure of the progress of reionization is the evolution of the globally-integrated mean 21-cm signal. In Figure 3 we show how the mass-weighted ionized fraction x_m and the mean differential brightness temperature, δT_b evolve against observed frequency, ν_{obs} for f2000, f2000C and f250. The first thing to note is that the reionization is significantly delayed, by $\Delta z \sim 1$ compared to f2000, when the small-scale clumping of the gas is included (f2000C), and even more so, by $\Delta z \sim 2$, when the ionizing sources are less efficient photon producers. Accordingly, the mean signal disappears and becomes undetectable at frequencies above ~ 110 MHz in f2000, but does so at much higher frequencies, ~ 120 MHz (~ 135 MHz) in f2000C (f250). At face value this seems to imply that our f2000 reionization history will be impossible to observe in places with high FM interference, as is the case with e.g. LOFAR and GMRT, which operate above 115 MHz, but as we will show below, this is probably a too simplistic conclusion.

It has been proposed that one could possibly detect the transition from fully-neutral gas to almost fully-ionized as a “global reionization step” over the whole sky (Shaver et al. 1999). To be detectable against the smoothly varying foregrounds, such a transition should occur fairly quickly, resulting in a sharp drop in the global 21-cm signal in frequency space when observed with a single dish radio telescope. All of our models show a rather gradual transition, with the mean signal decreasing by ~ 20 mK over ~ 20 MHz. Detecting such a transition is in principle well within the capabilities of even a 10 m radio dish (Shaver et al. 1999). However, a gradual change over 20 to 30 MHz would be difficult to disentangle from the strong foregrounds. The practicality of such observation would thus depend strongly on the (still highly-uncertain) detailed properties of the spectral index variations of the foregrounds and how well one can model and subtract them.

5 REIONIZATION GEOMETRY SEEN IN REDSHIFTED 21-CM EMISSION

5.1 Global evolution

We start with an overview of the progress of reionization in our simulations f2000 and f250, as seen in the 21-cm emission line. We present a visualization of the evolution of the differential brightness temperature in Fig. 4. We constructed these slices by linearly interpolating the evolution of the whole simulation box between our discrete time outputs, wrapping the box periodically after each complete crossing of the volume, and taking slices through the resulting long box. The vertical axis corresponds to the complete extend of our simulation volume of $100 h^{-1}$ Mpc comoving, while the horizontal axis shows the redshift at that position. Since redshift corresponds to frequency, these slices are equivalent to slices through an idealized observational image-frequency volume. We took the slices at an angle to the simulation cube axes, to avoid artificial periodicity effects caused by repeatedly passing through the same structures at later times. We also include the effect of peculiar bulk velocities from our N-body simulations, which result in redshift distortions along the line-of-sight (see Sect. 6.2 for more discussion on this last point).

Both slices show all the basic evolution trends we discussed in Paper I. The reionization starts around $z \sim 20$, with a few isolated and highly clustered ionized regions. Most of the gas is still neutral and quite bright at 21-cm emission, with some pixels reaching δT_b of well over 100 mK. The Cosmic Web is already well-developed and shows in the images even at these fairly large scales. For f2000 (Figure 6, top image) the first H II regions quickly merge with each other locally, forming significantly larger ones, of size ~ 10 Mpc comoving, already by $z \sim 14$, while at the same time many new ionizing sources emerge and start expanding their own local H II regions. By redshifts $z \sim 12.5$ many of the larger H II regions merge together to form a couple, and later on just a single, very large and topologically-connected (but highly-nonspherical) volume of $> 10^4$ (Mpc) 3 . Essentially all remaining ionized regions merge with this large one around $z \sim 11.5$ and the last pockets of neutral gas (mostly in the large voids, which have no local ionizing sources and are fairly far away from any source) are ionized by $z \sim 11$. In the f250 case (Figure 6, bottom image) the evolution is a bit slower due to the weaker sources, and the H II regions initially smaller, on average. Essentially the same main evolutionary trends remain in force, with significant local overlap of H II regions starting at $z \sim 12$, and the wide-spread merging of these between redshift $z = 11$ and 11.5. These finally merge into one huge ionized region between $z = 10$ and 9.5, although significant local pockets of neutral gas remain until the end.

While these features are generic and thus seen in all slices, there are a number of special features to note. Reionization is a highly inhomogeneous process, with large variation in its progress between different 2D slices of the same simulation, and even more between different lines-of-sight (LOS). For example, in the f2000 slice some LOS contain only few 21-cm features after $z \sim 13$, while others going through neutral pockets until, and even after global overlap (defined as the time when the mass ionized fraction drops below 1%). In the f250 case similar LOS behaviour can be seen. This strong patchiness until late times will have important implications for direct observations of high-z Ly- α sources, a point we will address in future work.

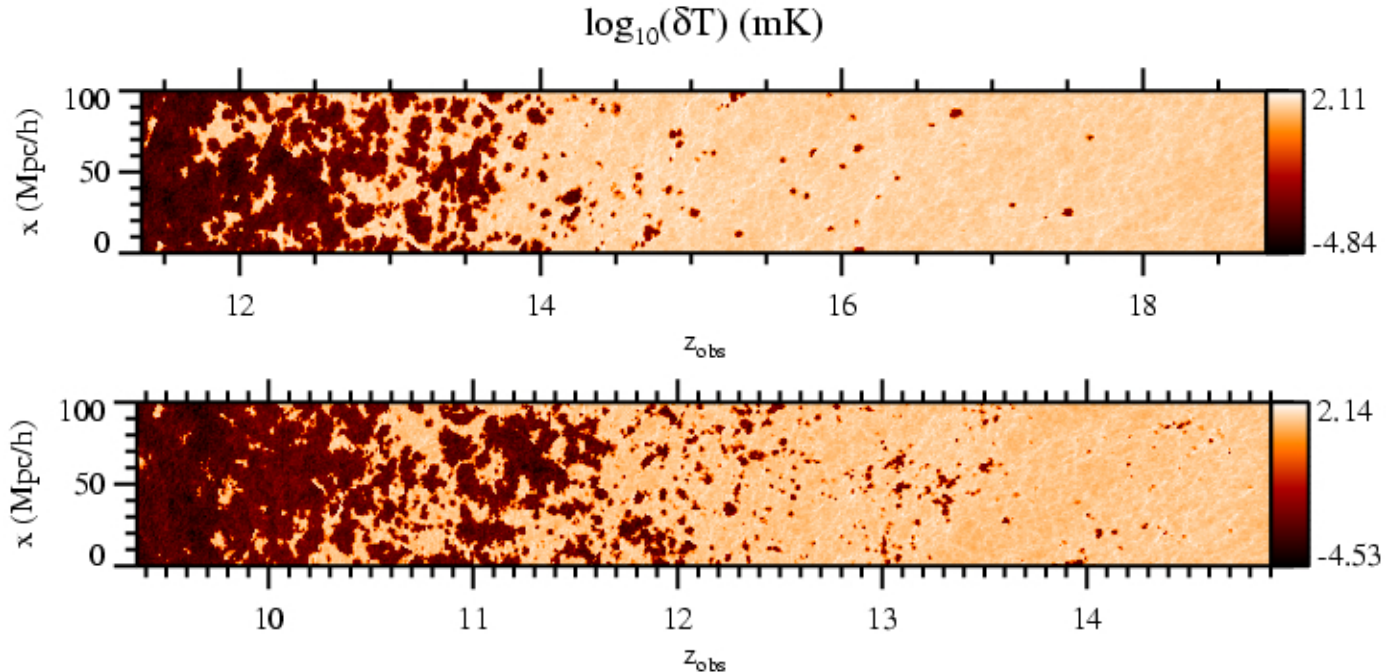


Figure 4. Position-redshift slices from the f2000 (top) and f250 (bottom) simulation. The spatial scale is in comoving units. These slices illustrate the large-scale geometry of reionization seen at 21-cm and the significant local variations in reionization history. Observationally they correspond to slices through an image-frequency volume.

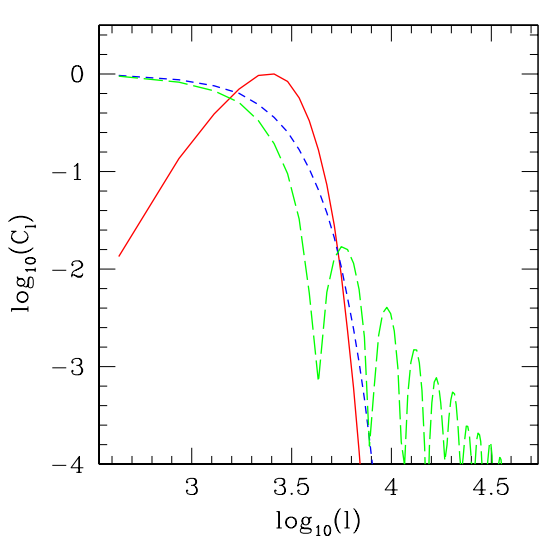


Figure 5. Angular power spectra of the compensated Gaussian (red/solid), Gaussian (short-dashed/blue), and tophat (long-dashed/green) beams all with FWHM of 3 arcmin and each normalized to maximum of 1. The sharp cut-off of the tophat beam produces high ℓ oscillations, showing that it should not be used for Fourier analysis of results. The compensated Gaussian, which is the one most closely resembling real-life interferometer beams has less power at low ℓ 's than the Gaussian, reflecting to the relative insensitivity of compact interferometers for large scale structures.

5.2 Sky maps

In what follows we approximate the synthesized beam of angular size $\Delta\theta$ with a compensated Gaussian filter, given by

$$W_{\text{CG}}(\theta) = \frac{1}{2\pi\sigma^2} \left(1 - \frac{\theta^2}{2\sigma^2}\right) \exp\left(1 - \frac{\theta^2}{2\sigma^2}\right), \quad (9)$$

with a FWHM equal to $\Delta\theta = 2\sigma\sqrt{2(1 - \text{LambertW}(e/2))}$ ($\text{LambertW}(e/2) \approx 0.685$). The compensated Gaussian has a shape in Fourier space whose real part, $k^2 \exp(-k^2/2)$, approximates well the actual observational beam shape of a compact interferometer (often referred to as ‘dirty beam’), being insensitive to large scale features. For this reason we use the compensated Gaussian in most of our analysis. Its average value is zero, with a Gaussian-type peak in the middle, surrounded by a negative through. As a consequence, data convolved with this beam will have both positive and negative values. In some cases we also use two other beam shapes, a Gaussian with FWHM of $\Delta\theta$ and a top-hat function of width $\Delta\theta$. These two beam shapes are simple and widely used in the literature. We use them in a few cases below, and when we do so we explicitly specify it. For reference we show plots of the angular power spectra of all three beam types in Fig. 5. The frequency bandwidth integration is always done with a tophat function, which is generally a good approximation to the actual integration used in observations.

In Fig. 6 we show sample ‘thick’ slices from f2000 of the density fields (green/white) with the ionized regions shown in blue, at three redshifts. A thick slice contains the average of several slices corresponding to a given band in frequency, to allow comparison to the images of finite bandwidth below. We show thick slices for redshifts $z = 16.08$, early in the evolution (mass-weighted ionized fraction $x_m = 0.026$), at $z = 13.62$ when the volume is about half-ionized ($x_m = 0.52$), and at $z = 12.57$, when most of the volume is already ionized, but significant neutral gas patches still remain ($x_m = 0.80$). Below each of those slices we show the corresponding 21-cm emission maps, each integrated over a bandwidth $\Delta\nu = 200$ kHz and convolved with a compensated Gaussian

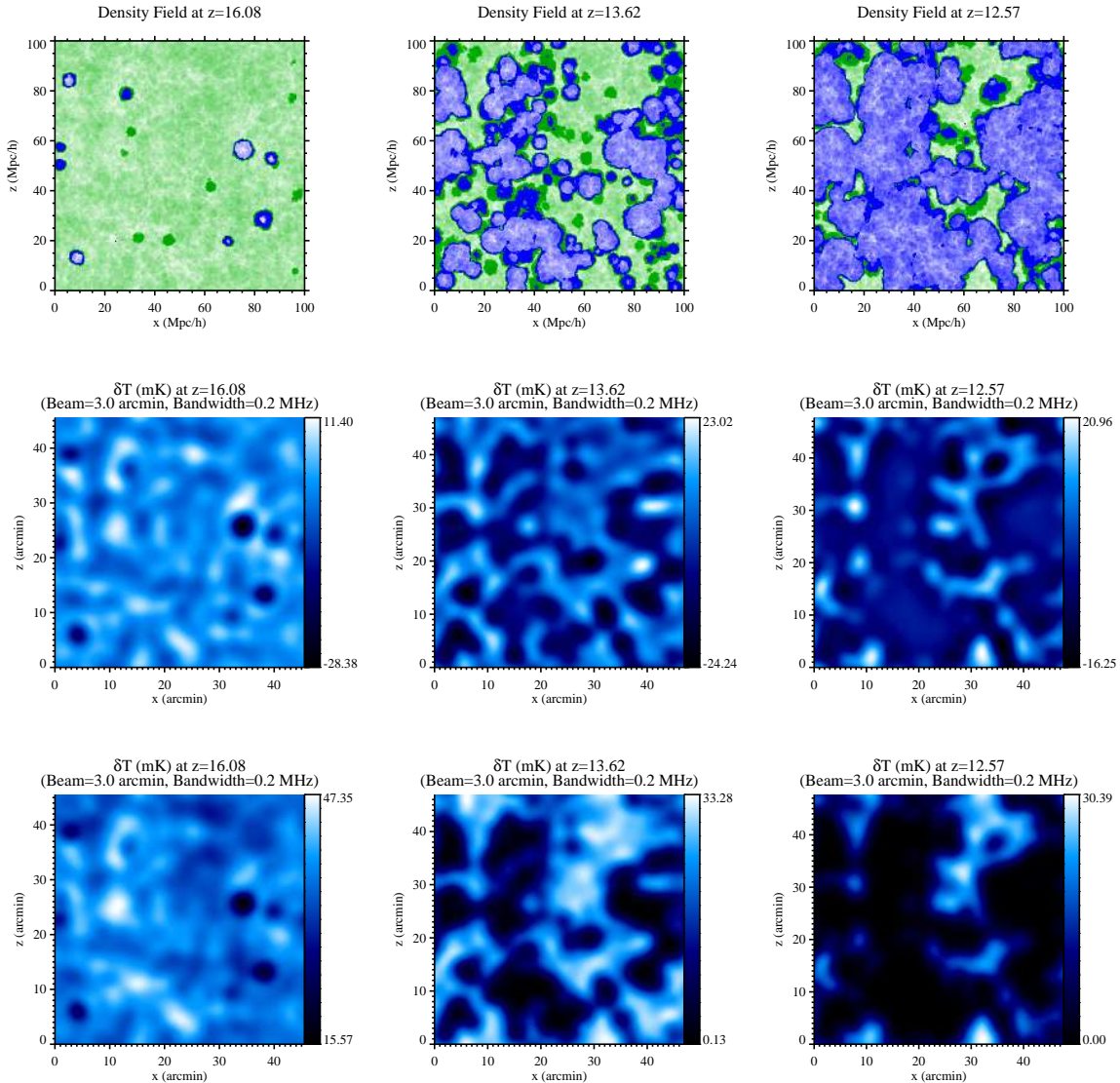


Figure 6. The topology of reionization seen at redshifted 21-cm line at redshifts $z = 16.08, 13.62$ and 12.57 for f2000. Top row panels: a thick slice (corresponding to 0.2 MHz in frequency) showing H II regions (blue) superimposed on the density field (green). Middle row panels: The same reionization topology as seen at 21-cm with $3'$ FWHM compensated Gaussian beam and 0.2 MHz bandwidth. Bottom row panels: The same as the middle panels, but with a Gaussian beam of the same FWHM.

beam of FWHM $3'$. The third row shows the images for a Gaussian beam of the same FWHM. For simplicity, when integrating over the bandwidth we neglected the redshift evolution over that bandwidth, which is justified for such small $\Delta\nu$. As explained above, the compensated Gaussian beam produces negative values since its average is zero.

An important point to note is that while the minimum and maximum values change over time, the full range from the brightest to the least bright pixel in this redshift interval is roughly independent of the redshift and remains around 30 mK for a Gaussian beam and around 40 mK for a compensated Gaussian. However, this is not the case very early, when the reionization has barely started and much later, close to overlap; in at those times the fluctuations are less pronounced. This happens because during these

epochs the fluctuations are mostly dictated by the fluctuations of the underlying density field, rather than by the patchiness of reionization, which strongly dominates the fluctuations at the intermediate times. The images illustrate how well the density fluctuations and the H II regions would show on a realistic 21-cm sky map. In spite of the significant level of smoothing, all large-scale features remain clearly visible in the maps. The larger H II regions are apparent as holes in the 21-cm radiation, and the neutral density peaks correspond to strong emission peaks. Some smaller, isolated ionized regions, with sizes below the beam smoothing length disappear from the map, particularly for the Gaussian smoothing. However, both the density fluctuations in the neutral regions and the large-scale patchiness of reionization remain clearly visible. The compensated Gaussian has much less power on large scales than the

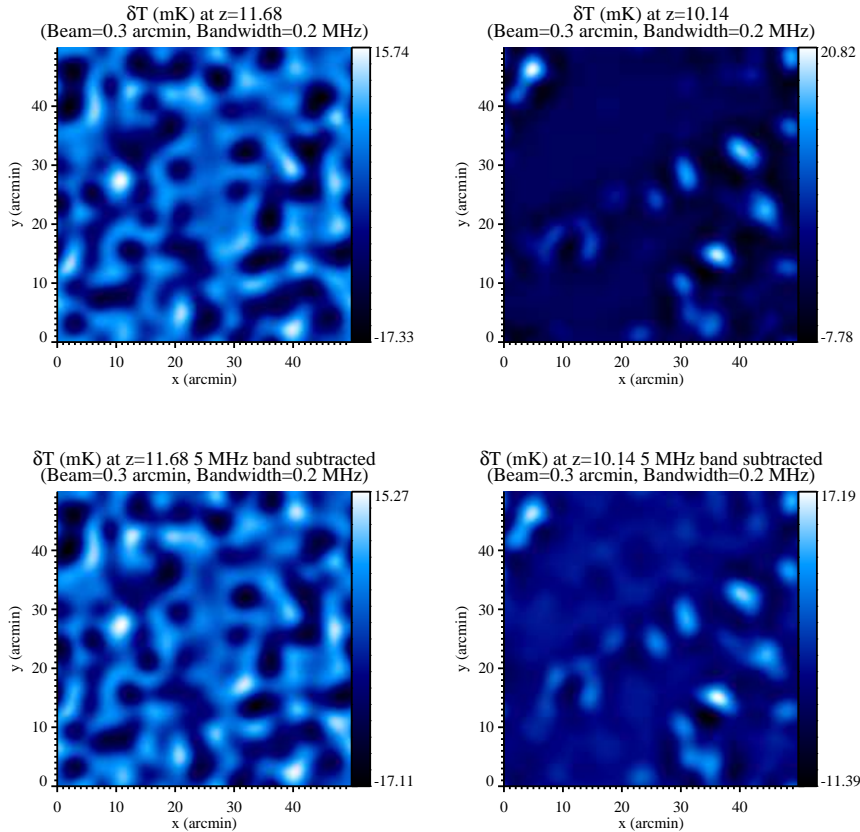


Figure 7. (top) Sample 21-cm sky maps at redshifts $z = 11.68$ and 10.14 from f250 and (bottom) the same maps, but after subtracting a wide, 5 MHz band from it. Subtracting the signal from such a wide band should remove most of the foregrounds without affecting the underlying redshifted 21 cm signal.

Gaussian beam, but more power on smaller scales, and therefore shows the detailed features better. The weaker 21-cm signatures of the mostly-ionized structures inside the H II regions are washed away and would require significantly higher spatial resolution and sensitivity in order to be detected.

Although obtaining images of 21-cm emission would be the ideal observational result it is not expected that such maps will be easily extracted in the near term, due to the sensitivity limits of the planned observations, and especially due to the strongly dominant foregrounds. In order to eliminate the foregrounds effectively one has to make use of their frequency characteristics. The issues of foregrounds is a complicated one, and goes beyond the scope of this paper. However, as a first approximation, the foregrounds can be assumed to be a slowly-varying power-law in frequency and to have smooth angular variations. Thus, as a first step, we can simply subtract the mean signal over a given band $\Delta\nu$. Here we take $\Delta\nu$ to be 5 MHz. Such an approach would average out any small random variations of the spectral index, as well as subtract the main, power-law-like component.

Figure 7 shows two sample maps (using a compensated Gaussian beam; top images) and the corresponding maps with a 5 MHz band subtracted (bottom images). These correspond to the half-ionized point ($z = 11.68$, left panels) and the late phase ($z = 10.14$, right panels) of our f250 simulation. The subtraction process leaves the structures showing on the map largely intact, demonstrating that such a subtraction procedure would not affect the signal substantially, while at the same time eliminating much of the fore-

grounds. How well such procedure would work in practice would of course depend on how well-behaved the foregrounds are.

Obtaining detailed 21-cm sky maps would give us a very rich set of data on both early structure formation and the progress of reionization. However, extracting these from the noisy data dominated by strong foregrounds will not be easy. Thus, in the following sections we first consider the detectability of individual large features and then statistical measures of the expected signal, both of which should be significantly easier to obtain from the observational data, and so should be the first goal of the observations.

6 INDIVIDUAL FEATURES

6.1 Rare, bright peaks

The brightest emission peaks for a given beam and bandwidth are possibly the 21-cm emission features easiest to detect. In Figure 8 we show the maximum pixel value of the differential brightness temperature, $\Delta T_{b,max}$ versus redshift z for beam-sizes and bandwidths $(\Delta\theta_{beam}, \Delta\nu_{bw}) = (6, 0.4)$ (roughly corresponding to the ones relevant to PAST), $(3, 0.2)$ (“LOFAR”), $(1, 0.1)$ (“SKA”) and the full resolution of our simulation (corresponding to single cells), where the beam sizes are in arcminutes and the bandwidths are in MHz. In order to compare to the mean signal and the signal without reionization, we use a Gaussian beam here, since the compensated Gaussian has a zero mean by definition.

The first thing to note is that the values and the shape of the

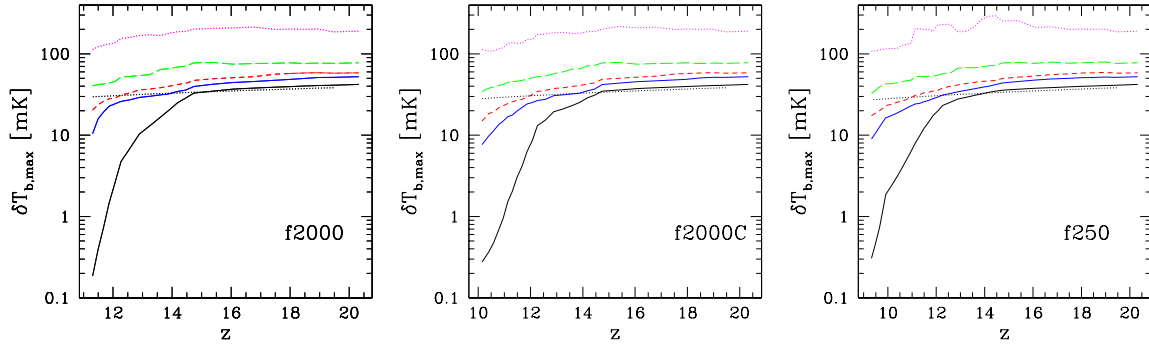


Figure 8. The brightest peak in the simulation box as a function of redshift, for (from left to right, simulations f2000, f2000C, f250, as labelled). Shown are the maximum pixel value of the differential brightness temperature, $\delta T_{b,\max}$ vs. redshift z for several beam-sizes and bandwidths, as follows, $(\Delta\theta_{\text{beam}}, \Delta\nu_{bw}) = (6, 0.4)$ (blue, solid), $(3, 0.2)$ (red, short-dashed), $(1, 0.1)$ (green, long-dashed) and the full resolution of our simulation (i.e. corresponding to single simulation cells; magenta, dotted), where the beam sizes are in arcminutes and the bandwidths are in MHz. For reference we also show the mean differential brightness temperature over the whole box (thin, black, solid) and the same, but if the gas were fully-neutral (i.e. if no reionization occurred; thin, black, dotted).

curves do not depend significantly on the reionization history, except for a shift in redshift, by about $\Delta z = 1.5$ (2) between f2000 and f2000C (f2000 and f250). The magnitudes of the brightest peaks is fairly high, at several tens of mK even in the beam- and bandwidth-smoothed cases, and well over 100 mK for full resolution. The magnitudes generally drop with redshift, but only mildly and the curves stay largely flat over the whole redshift range. The higher resolution and sensitivity of SKA would provide a significant improvement, while the difference in the signal between the LOFAR and PAST scales is rather marginal.

These brightest peaks generally correspond to high-density, still neutral regions, i.e. regions that are on the verge of forming galaxies, who in turn would start ionizing their surroundings. Hence, while the magnitude of the peaks do not vary much with redshift, the location in the box at which it is found does vary significantly and the brightest peaks at one redshift become deep troughs at later times. For reference we also show the mean simulated 21-cm emission signal, as well as the mean signal if we assume the volume to be completely neutral (i.e. if reionization never happened). The mean signal from the box is well below the maximum one at all redshifts, even for maximum smoothing, and it decreases much more steeply with redshift, thus the difference from the peaks grows significantly with time, from factors of 1.2-6 (depending on the smoothing) at $z \sim 16$, up to 35-320 at late times ($z \sim 11.5$). Notably, the peak signals are also generally higher than the mean signal for a neutral volume. This indicates that the peak signals always come from overdense regions, even though, as we showed in Paper I, the reionization is clearly inside-out, i.e. the high-density peaks get ionized preferentially compared to the voids. For high levels of smoothing (i.e. large beam sizes and bandwidths) the peak signal drops below the corresponding fully-neutral gas signal since by that time our volume is more than half-ionized and hence any beam that samples much of the box would inevitably include significant ionized regions. This is a consequence of the high bias of the density peaks (and sources) at high redshift, which means that the maximum-signal peak inevitably is close to other density peaks that have been ionized already.

Searching for the relatively rare, bright peaks could thus be an efficient way to detect the signatures of reionization, even in its late stages when the universe is already more than 99% ionized. This would make these stages observable to radio arrays which are

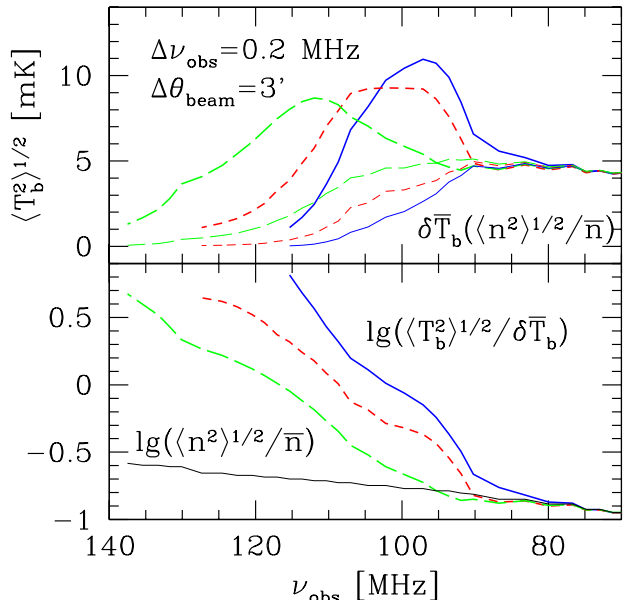


Figure 11. (top) Rms fluctuations of the differential brightness temperature, $\langle \Delta T_b^2 \rangle$ vs. observed frequency, ν_{obs} for f2000 (solid, blue), f2000C (short-dashed, red) and f250 (long-dashed, green). We also show the corresponding $\delta \bar{T}_b (\langle n^2 \rangle^{1/2} / \bar{n})$, i.e. the temperature fluctuations if they were following the fluctuations of the density, normalized to their respective means (thin lines, same line types and colours for the cases). (bottom) the density (thin, solid, black) and differential brightness temperature fluctuations relative to their respective means (thick lines, same line types and colours for f2000, f2000C and f250 as in the top panel) vs. frequency.

strongly affected by interference in the FM-band, such as LOFAR and the GMRT, since they correspond to frequencies well above the FM band. The statistics of these rare events is discussed in Sect. 7.3.

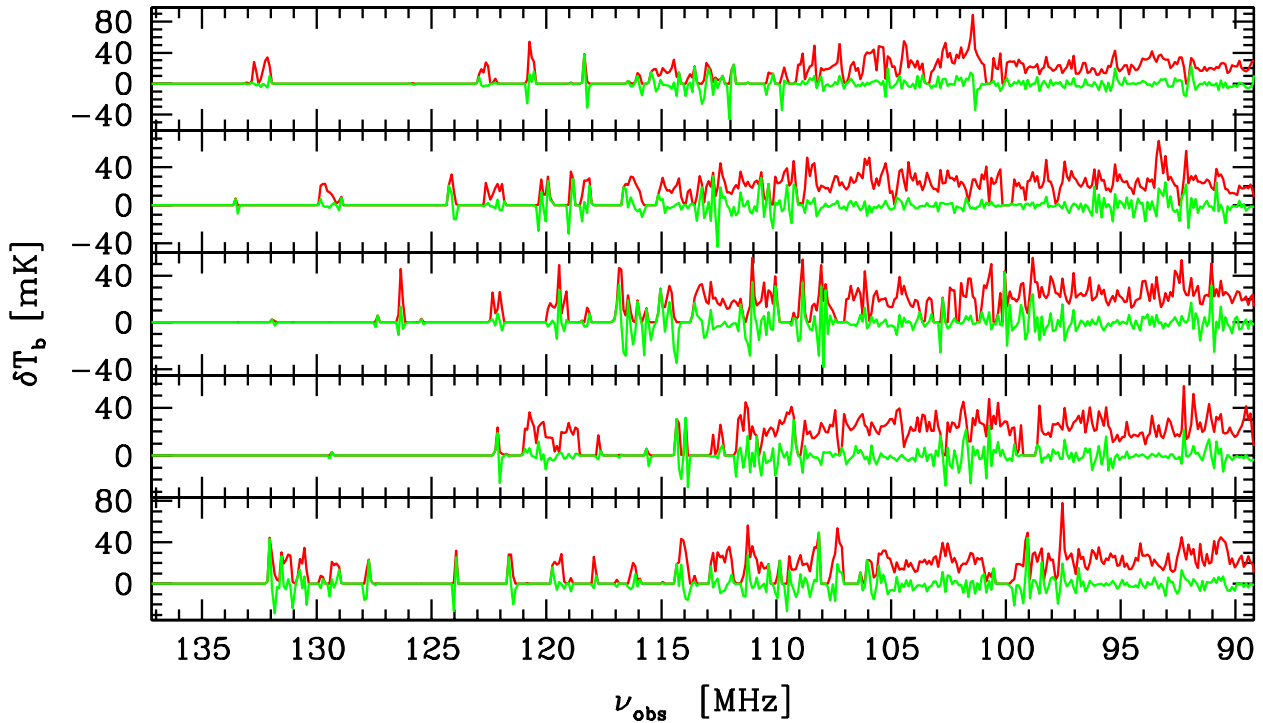


Figure 9. Sample line-of-sight 21-cm spectra obtained from our simulation data (simulation f250). The figure shows the redshift distorted spectra (red) and the difference between the distorted and the undistorted spectra (green).

6.2 Line-of-sight spectra

Next we present line-of-sight (LOS) 21-cm emission spectra obtained from our simulations. These can in principle probe in detail the neutral structures at high-redshifts along that LOS, as well as detect the H II regions as deep troughs in the spectra. In order to obtain spectra over large frequency bands we use the technique discussed in Sect. 5.1 for deriving the evolution over the complete redshift and time intervals of our simulations. We present the full-resolution spectra (essentially just LOS cuts through the data shown in Fig. 4), as well as the corresponding beam- and bandwidth-smoothed spectra for our simulation f250, since its overlap is latest, thus it extends furthest into the most easily observable redshift range.

The full-resolution (at resolution ~ 30 kHz, corresponding to one computational cell) spectra are shown in Figure 9. The red line shows the spectra including redshift distortions due to the bulk peculiar velocities, and the green line is the difference between the distorted and undistorted spectra. The redshift distortions introduce substantial changes in the spectrum, moving peaks to different frequencies (showing up in the difference as a deep dip next to a high peak), merging the emission of some gas parcels, and spreading others out over a larger range in frequency. The comparison shows that these are noticeable effects that should always be taken into account. These redshift distortions can in principle be used to derive information about the underlying cosmology as well as about reionization (Barkana & Loeb 2005a; McQuinn et al. 2005), but this falls outside the scope of the current paper.

As was also noted above, at high resolution there are some

very bright pixels, with $\delta T_b > 50$ mK, and these are fairly common during most of the evolution, and generally at least one is found on every LOS. However, they become increasingly rare after $z \sim 12$ ($\nu_{\text{obs}} \sim 110$ MHz), since by that time most of the high-density peaks have formed ionizing sources. Conversely, at about that time the H II regions become common and start to be seen along most LOS as deep troughs. The size of these troughs initially corresponds to the typical size of the ionized regions, ~ 10 Mpc comoving, or about 0.5 MHz. As discussed in detail in Paper I around the time the volume is half-ionized these ionized regions quickly start merging with each other and start forming much larger ones, seen here as wider troughs, of several MHz each. Most of the signal eventually disappears as the volume becomes ionized. However, as we already pointed out, this occurs at quite different frequencies along different LOS. Along some LOS there are essentially no neutral structures for $\nu > 120$ MHz, while along others significant neutral regions persist until $\nu \sim 135$ MHz or later.

These fairly sharply-defined H II regions suggest a local (on scales tens of Mpc) equivalent of the “Global step” discussed in Sect. 4. While the last proved rather gradual, on a more local level the steps are be quite steep, from 30-50 mK down to almost 0 and back within a fraction of a MHz.

In Figure 10 we show the effect of beam- and bandwidth-smoothing on the spectra. The beam we use is again the compensated Gaussian, which produces negative differential brightness values at the minima. Clearly the smoothing reduces the signal considerably when most of the material is still neutral ($\nu \lesssim 100$ MHz), and the fluctuations are entirely due to density fluctuations, at relatively small scales. Once the first H II regions begin to expand, they

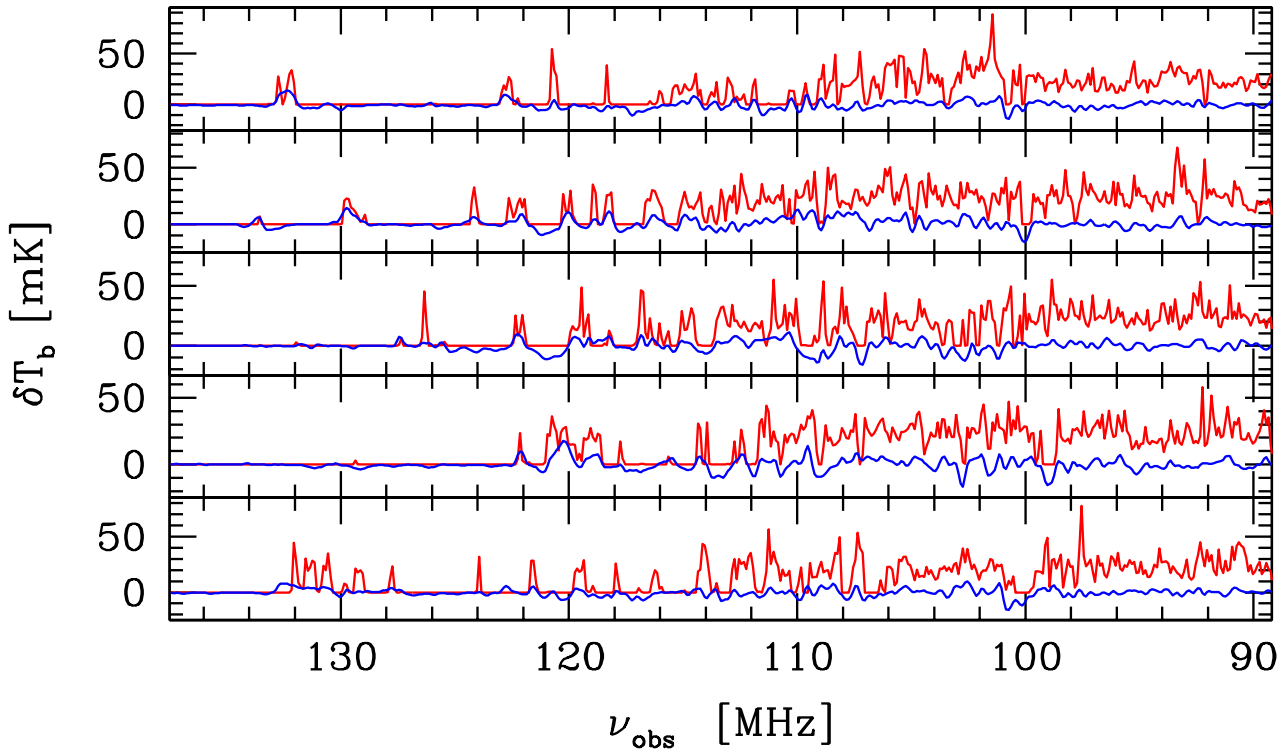


Figure 10. Sample line-of-sight 21-cm spectra obtained from our simulation data (simulation f250). Shown are the full-resolution (red) and the beam- and frequency-smoothed spectra (blue). For the latter we used a compensated Gaussian beam with a FWHM of 3' and a bandwidth of 0.2 MHz.

produce much stronger fluctuations. These show up in the spectra, although the smallest ones are still averaged out by the smoothing. The valleys corresponding to the H II regions are generally deeper than the neutral density peaks, so are in principle easier to detect features. At later stages the isolated peaks are suppressed in some cases, but often remain clearly visible, depending on their characteristic size and environment. For these LOS and smoothing the signal does never vary more than a few tens of mK, but the main features of the unsmoothed data are preserved and should still be detectable.

7 STATISTICAL SIGNALS

7.1 Spatial rms fluctuations

The prominent individual 21-cm features we discussed in the previous section, either rare, bright emission peaks or large individual H II regions would quite possibly be the first signatures of the reionization epoch to be seen. Once such a first detection is made the next aim would be to put more robust constraints on the progress and duration of reionization than the ones currently available. At the next level of complexity, the data may be used to derive the statistical measures of the fluctuations in the 21-cm signal. This could be achieved by considering a number of observational fields, thus suppressing the noise and systematics in the foregrounds.

The fluctuations of the 21-cm EOR signal can come from several sources. Here we concentrate on the dominant effect, the large-scale patchiness of reionization. The fluctuations can be derived as

a single number (rms), for any given scale (defined by the observational beam and bandwidth), or in more detail in the form of angular power spectra. We consider both here, starting with the rms fluctuations. The rms fluctuations are the equivalent of the global step discussed in Sect. 4, but observed with an interferometer (which is insensitive to a mean global signal).

In Fig. 11 we show how the fluctuations in the mean signal change with redshift/frequency (top panel) for f2000, f2000C and f250. These were calculated using a top hat beam of 3' and a bandwidth of 0.2 MHz. The top hat was used here for computational convenience, using a different beam would change the numbers slightly, but would not affect the basic trends which we want to illustrate here. Early-on the 21-cm fluctuations closely follow the gas density fluctuations, since very little of the gas is ionized. Once some more substantial ionized patches start appearing, with sizes roughly of order of the beam- and bandwidth smoothing, the differential brightness temperature fluctuations quickly raise and reach a maximum of $\langle \delta T_b^2 \rangle^{1/2} \sim 10$ mK, after which they drop as more and more of the universe becomes ionized, reaching ~ 1 mK at overlap. This behaviour is quite generic and occurs in all cases presented here. However, the frequency, ν_{\max} (and redshift) at which the maximum of the fluctuations is reached varies significantly among the runs, from $\nu_{\max} \sim 97$ MHz for f2000 up to $\nu_{\max} \sim 112$ MHz for f250. The peak value of the fluctuations varies modestly between the models, from 11 mK for f2000, down to 8.7 mK for f250. In all three cases the peak fluctuations occur at the time when the universe is $\sim 50\%$ ionized by mass. The peaks are roughly symmetric in all cases and significantly wider for the late-overlap scenario (f250) than for the early-overlap one (f2000).

As a reference we also show the $\delta\bar{T}_b(\langle n^2 \rangle^{1/2}/\bar{n})$, i.e. the fluctuations for reionization scenarios with the same $\delta\bar{T}_b(z)$ as the actual simulations, but assuming that the process occurred homogeneously rather than patchily. In this last case the fluctuations of the emission would have been solely due to the fluctuations in the underlying density field. Clearly the patchy reionization creates substantial extra power over a wide range of frequencies. The difference is especially large close to overlap, where the mean signal essentially disappears, while the actual patchy signal is ~ 1 mK even at overlap, when the mass ionized fraction is less than 1 per cent. The bottom panel underlines this point further by showing the rms fluctuations of the differential brightness temperature relative to its mean, $\langle \delta T_b^2 \rangle^{1/2}/\delta\bar{T}_b$, for f2000, f2000C and f250, and the same for the density fluctuations, $\langle n^2 \rangle^{1/2}/\bar{n}$ (where the last is the same for f2000, f2000C and f250, since they use the same underlying density field). We see that the relative differential brightness temperature fluctuations are more than an order of magnitude larger than the relative fluctuations of the underlying gas density field.

As in the case of the global step, a sudden decrease in the rms fluctuations should be easier to detect observationally. Our f2000 simulation does indeed shows a fairly steep drop over 15 MHz after the peak (but located in the FM band), whereas the f2000C and f250 cases display a more gradual change over 20 MHz and 30 MHz, respectively, making them in principle harder to detect.

7.2 Power spectra

The quantity closest to the actual radio array observational data is the 2D angular power spectrum. It shows how the power of the fluctuations is distributed over the different angular scales. We follow the convention used in CMB analysis and construct the angular power spectrum expanded in spherical harmonics, $[\ell(\ell+1)C_\ell/2\pi]^{1/2}$, where $\ell = 2\pi/\theta$, with the angle θ in radians. The results are shown in Figure 12 for simulations f2000 and f250 (solid lines). For reference we also show the corresponding angular power spectra of the underlying density field (dotted lines). These power spectra were constructed at full resolution without any beam- or bandwidth smearing, since these are instrument-specific. The smallest value of ℓ at which we calculate the power spectra corresponds to half of our box size, since below that there is an unphysical damping due to the finite simulation box size. The largest ℓ value shown corresponds to one computational cell and thus is related to our spatial resolution.

The power spectrum at redshift $z = 20.3$ is identical to that of the underlying density field, since at that time there are only a few, small H II regions. In both reionization histories, evolution of the power spectrum proceeds by a rise at small scales (large ℓ), shifting slowly to larger scales as reionization reaches the 50% point, and followed by a decline of the power as most of the universe gets ionized. The declining power spectrum keeps peaking at approximately the same ℓ value as when it was at its maximum, but the distribution becomes quite broad. Comparing the f2000 and f250 cases shows that the f250 case peaks at somewhat smaller scales ($\ell \approx 5000$, $\theta \approx 4'$) than the f2000 case ($\ell \approx 4000$, $\theta \approx 5'$). The f250 distribution is also somewhat broader with a slightly lower peak value.

This evolution of the power spectrum reflects the evolution of the H II regions. Initially they are small, but dominate the fluctuations, resulting in more fluctuation power at high ℓ . The maximum then moves to lower ℓ as the H II regions grow with time. As we showed in Paper I this growth levels off at a certain size (~ 10 Mpc for f2000) because once an ionized bubble grows larger than that

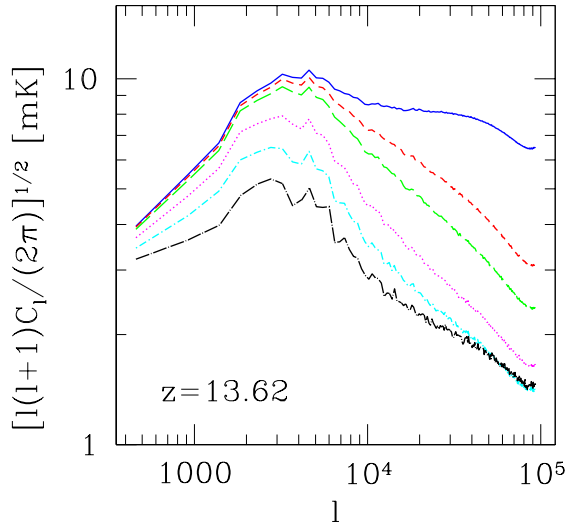


Figure 13. Angular power spectra $[\ell(\ell+1)C_\ell/2\pi]^{1/2}$ at $z = 13.62$ for f2000_406 and using bandwidths (top to bottom) 1 cell, 0.1 MHz, 0.2 MHz, 0.5 MHz, 1 MHz, and 2 MHz. This illustrates the effect on the power spectrum of integration over a given bandwidth.

size it merges with many other bubbles to form much larger ionized regions. This reflects a typical correlation length between source clusters, convolved with the source efficiency (number of ionizing photons produced per atom). The last is reflected in the f250 power spectra peak being at lower scales (higher ℓ). These very large bubbles which result from the mergers of multiple smaller ones are rare, however, and locally they partly retain the shapes and sizes of the original smaller bubbles which merged (see e.g. Figure 1), so the typical fluctuation size at the scales under consideration (sub-degree) is still dictated by the typical size (~ 10 Mpc) of bubbles resulting from local source clustering.

The power spectra magnitude grows strongly during the initial, very patchy phase of reionization, in all cases reaching a maximum of ~ 10 mK around the time of 50% ionization, in complete agreement with the results from the rms fluctuations we discussed above in Sect. 7.1. This is substantially over the power contained in the density field, about a factor 2 for the f2000 case, and 1.5 for the f250 case. At late times ($z < 12.3$ for f2000) the power spectra are significantly depressed due to the small neutral fraction remaining, with the peak value reaching only up to 1-2 mK. The broadness of the peak indicates that the power is contained in ever larger structures.

We do not show how beam smoothing affects the power spectra as this can be easily derived by multiplying the power spectrum with that of the beam (Fig. 5), and for detailed observational predictions this should be done with the “dirty beam” of the particular array under consideration. Both the Gaussian and compensated Gaussian beam will introduce an effective cut-off at the FWHM angle. Considering the multipole values for the peaks which we find, this means that planned experiments may be just sufficient to capture the expected peaks. Note that our results differ somewhat from the previous analytical estimates in (Zaldarriaga et al. 2004) who find larger structures dominating around the epoch of reionization, and the power spectra peaking at $\ell \sim 3000$. More importantly, their semi-analytical model predicts that the peak ℓ first decreases, from $\sim 10^4$ to ~ 3000 around the time of maximum signal, and then the

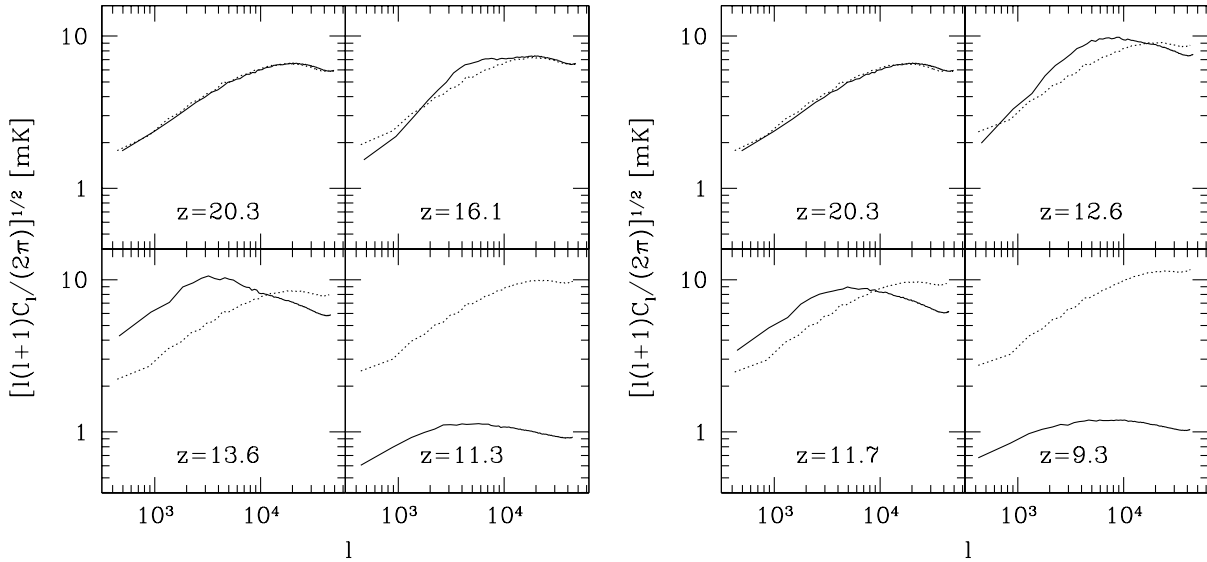


Figure 12. 2D angular power spectra of the differential brightness temperature fluctuations (solid lines) for f2000 (left) and f250 (right). For reference we also show the corresponding fluctuations if there were no reionization (i.e. due just to the fluctuations of the underlying gas density field assuming all the gas were neutral).

characteristic scale decreases again, with ℓ rising to $\sim 8,000$. This divergent behaviour reflects the differences in their prescription for the growth of bubbles and our simulations.

The bandwidth smoothing can in principle be derived by applying the appropriate window function to the 3D power spectra. Qualitatively, bandwidth smoothing takes away power at the high ℓ values since it will average of small bubbles along the line of sight. To illustrate the effect we show in Fig 13 how bandwidth smoothing affects the power spectrum at $z = 13.62$ for the f2000_406 case. The bandwidth varies from about 30 kHz (one cell) up to 2 MHz. Without smoothing the peak is at $\ell \sim 4000$, moving to larger scales for larger bandwidths. However, both the magnitude and the position of the peak barely change for $\Delta\nu \leq 0.2$ MHz, staying close to the maximum value of 10.3 mK. For the maximum bandwidth considered, 2 MHz, the peak value drops by almost a factor of 2, to 5.46 mK, and occurs at $\ell \sim 3000$. As expected, even modest smoothing washes out most of the small-scale power, but there is also some decrease of power on the larger scales, since we sample larger scales at which the fluctuations are lower.

7.3 Beyond the power spectra: non-Gaussianity of the 21-cm signal

The power spectra discussed in the previous section provide important information about the magnitude of the 21-cm fluctuations at different scales. However, they fall well short of a full description of the statistics of the 21-cm fluctuations, and the corresponding implications for high-redshift structure formation and reionization. Distributions with identical power spectra could have completely different properties and statistics. In Paper I we showed quantitatively for the first time that the PDFs of both the ionized gas fraction and the ionized gas mass are generally strongly non-Gaussian, even more so than the underlying density distribution, which starts Gaussian, but develops non-Gaussian features due to the forma-

tion of non-linear structures. Here we extend our results further by studying the PDF of the 21-cm differential brightness temperature.

We calculate the PDFs using the same method as in Paper I, in cubes of 5, 10 and $20 h^{-1}$ Mpc size and at two different redshifts for simulation f250, the first at the 50% ionization ($z = 11.9$) and the second during the late stages of reionization ($z = 10.8$). For the other simulations the PDFs are similar at the same ionization levels (which correspond to different redshifts due to the different reionization histories). The results are shown in Figure 14 (solid lines), along with the corresponding Gaussian distributions with the same means and widths (dotted lines). These Gaussian distributions are the ones one would construct on the basis of the power spectrum analysis. The PDFs are expressed in terms of deviations from the mean differential brightness temperature at that redshift.

These plots show that the PDFs of the 21-cm signal are highly non-Gaussian. Considering for instance the $5 h^{-1}$ Mpc case (blue lines) at $z = 11.9$, there is a 5-10 times larger probability for finding holes (corresponding to ionized regions) deeper than -10 mK from the average signal (which is 16 mK at that redshift) than expected from the Gaussian analysis. For the same 5 Mpc scale the peaks of 10 mK above the mean are also more frequent than the Gaussian statistics predicts, but higher peaks (> 12 mK) are actually more rare. The same trends are seen at larger scales (10 and $20 h^{-1}$ Mpc), although to somewhat lesser extent.

At the later redshift of 10.8, at which time the mean signal is 5 mK, there are very large over-abundances, by factors of up to 30, of holes of -6 to -2 mK. Even more interestingly, strong peaks of 10-20 mK above the mean signal are up to 1-2 orders of magnitude more abundant than the corresponding Gaussian predictions, and the distribution is even more skewed than at the earlier time. This over-abundance in the number of high peaks is roughly independent of the spatial scale considered, but occurs at different temperatures, from ~ 10 mK for $20 h^{-1}$ Mpc regions, up to 16-18 mK for $5 h^{-1}$ Mpc regions.

This shows that the even very late into reionization, when most

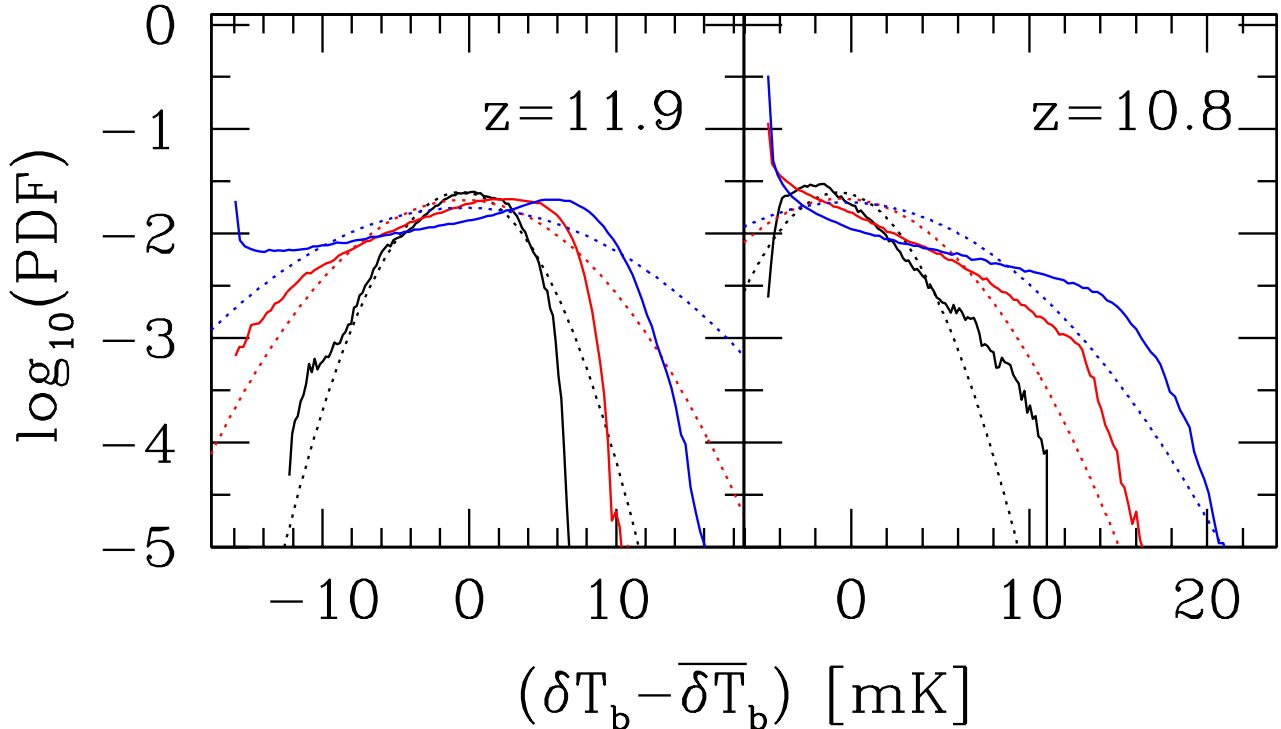


Figure 14. Non-Gaussianity of the 21-cm signal: PDF distribution of the 21-cm signal from simulation f250 for $z = 11.9$ (left) and $z = 10.8$ (right). The PDF were derived for cubical regions of sizes $20 h^{-1} \text{Mpc}$ (black solid), $10 h^{-1} \text{Mpc}$ (red solid), and $5 h^{-1} \text{Mpc}$ (blue solid). Also indicated are the Gaussian distributions with the same mean values and standard deviations (dotted, corresponding colours).

of the universe is ionized (for simulation f250 the mass ionized fraction is 84% at $z = 10.8$), there is still considerable signal available in isolated features. The results in Sect. 6.1 already hinted at this, and the non-Gaussian statistics puts numbers to it. The same behaviour is seen in all of our simulations, and should increase the chances of actually detecting the redshifted 21-cm line, even if reionization was mostly complete rather early.

8 CONCLUSIONS

We constructed the evolution of the redshifted 21-cm emission for several reionization histories resulting from large-scale radiative transfer simulations in a volume of $(100h^{-1} \text{ Mpc})^3$. This volume corresponds to ~ 1 degree on the sky and $\sim 5 - 10$ MHz in frequency, sufficient for capturing the scales relevant to reionization and its 21-cm signatures. We studied the various aspects of these 21-cm signatures, from the properties and statistics of individual bright features, to sky radio maps, to statistically-extracted signals. Our results can be summarized as follows.

We do not find a very sharp global step in the 21-cm signal resulting from the neutral gas being ionized and disappearing. Instead, the transitions we observed are rather gradual, with a ~ 20 mK decrement of the signal over ~ 20 MHz. A similar results if obtained for the change in rms fluctuations with frequency. Assuming well-behaved foregrounds, such a transition is well within the achievable instrument sensitivity and thus could still be detectable, though not as easily as a sharper transition would have been.

The large-scale geometry of reionization is well-resolved in 21-cm sky maps even after beam smearing. Such maps would show structures in the neutral IGM, as well as the shapes of the HII regions are the the sources, providing a unique window on early structure formation. We also showed that subtracting the average signal from a large frequency band (~ 5 MHz) should be efficient way to remove smooth foregrounds while leaving the 21cm fluctuations essentially intact.

Analyzing high-resolution LOS spectra we find that redshift distortions are considerable, and hence will influence the shapes of structures along the LOS, and should be taken into account when constructing 3D (position/frequency) observables from simulations. There is a large variation between different LOS in terms of the structures encountered and the time when the epoch of overlap is reached. If the foreground emission from galactic and extragalactic sources can be effectively removed, the fluctuations seen along the LOS would provide detailed information about the underlying neutral density field. However, the most easily detectable objects would be local ionized bubbles, which are bordered by sharp transitions, where the 21cm signal changes by tens of mK over very small intervals in frequency. We also presented for the first time simulated LOS spectra filtered with a realistic beam and bandwidth. These show that although small details are smoothed over and the signal variations are smaller than in the full-resolution spectra, the main structures remain clearly visible and should be detectable.

Statistical measures, such as fluctuations and the two-dimensional power spectra show that the fluctuations always reach a maximum when the gas is $\sim 50\%$ ionized by mass, and that the

power is boosted considerably (by a factor ~ 2) compared to the total density. At that maximum the power spectra show a clear peak at an angular scale of $\ell \sim 3000 - 6000$, depending on the particular reionization history. Earlier and later, the peaks are broader, indicating that more scales, both larger and smaller are involved. In order to be able to observe this peak the planned experiments should have a resolution of $\sim 3'$ or better.

The derived PDFs show that the 21cm signal is strongly non-Gaussian at all scales. In particular, at late times the chance of finding individual bright features can be 10 or more times above the Gaussian prediction. At all times the brightest point in our simulation volume is 20–60 mK for beam/bandwidth smoothing typical for the planned LOFAR/PAST/GMRT-type observations. This is insensitive to the particular reionization history. It is therefore likely that even in the case of early reionization, individual bright peaks can be observed at frequencies above 120 MHz.

Finally, we note that while we consider several specific reionization scenarios here, many of our conclusions appear to be quite generic, e.g. the significant boost of the 21-cm emission fluctuations due to reionization patchiness, the fluctuations reaching maximum at $\sim 50\%$ ionization by mass and declining thereafter, and the relative insensitivity of the magnitude and statistics of the brightest spots in the box. On the other hand, certain important features vary significantly among scenarios - e.g. at which redshift is the fluctuations peak reached. These depend on a number of still highly-uncertain reionization parameters. In the models discussed here we vary the most important of these parameters, the ionizing photon production efficiency of the sources and the level of gas clumping at small scales. As we discussed above, the ability to detect EOR signatures with any particular instrument would depend strongly on when these features occur.

ACKNOWLEDGMENTS

GM acknowledges support from the Royal Netherlands Academy of Art and Sciences. This work was partially supported by NASA Astrophysical Theory Program grants NAG5-10825 and NNG04GI77G to PRS. We thank P. McDonald, C. Hirata and S. Sethi for enlightening discussions, and TIARA for their hospitality and financial support.

REFERENCES

Allison A. C., Dalgarno A., 1969, *ApJ*, 158, 423
 Barkana R., Loeb A., 2005a, *ApJL*, 624, L65
 Barkana R., Loeb A., 2005b, *ApJ*, 626, 1
 Carilli C. L., Gnedin N. Y., Owen F., 2002, *ApJ*, 577, 22
 Chuzhoy L., Shapiro P. R., 2005, ArXiv Astrophysics e-prints (astro-ph/0512206)
 Ciardi B., Madau P., 2003, *ApJ*, 596, 1
 Field G. B., 1959, *ApJ*, 129, 536
 Furlanetto S. R., Sokasian A., Hernquist L., 2004, *MNRAS*, 347, 187
 Gnedin N. Y., Shaver P. A., 2004, *ApJ*, 608, 611
 Hirata C. M., 2005, *MNRAS*, in press (astro-ph/0507102)
 Iliev I. T., Ciardi B., Alvarez M. A., Maselli A., Ferrara A., Gnedin N. Y., Mellema G., Nakamoto T., Norman M. L., Razoumov A. O., Rijkhorst E.-J., Ritzerveld J., Shapiro P. R., Susa H., Umemura M., Whalen D. J., 2006, submitted to *MNRAS* (astro-ph/0603199)
 Iliev I. T., Mellema G., Pen U. L., Merz H., Shapiro P. R., Alvarez M. A., 2005, submitted to *MNRAS*, (astro-ph/0512187)
 Iliev I. T., Scannapieco E., Martel H., Shapiro P. R., 2003, *MNRAS*, 341, 81
 Iliev I. T., Scannapieco E., Shapiro P. R., 2005, *ApJ*, 624, 491
 Iliev I. T., Shapiro P. R., Ferrara A., Martel H., 2002, *ApJL*, 572, L123
 Iliev I. T., Shapiro P. R., Raga A. C., 2005, *MNRAS*, 361, 405
 Kogut A., Spergel D. N., Barnes C., Bennett C. L., Halpern M., Hinshaw G., Jarosik N., Limon M., Meyer S. S., Page L., Tucker G. S., Wollack E., Wright E. L., 2003, *ApJS*, 148, 161
 Kohler K., Gnedin N. Y., Miralda-Escudé J., Shaver P. A., 2005, *ApJ*, 633, 552
 Kuhlen M., Madau P., Montgomery R., 2006, *ApJL*, 637, L1
 McQuinn M., Zahn O., Zaldarriaga M., Hernquist L., Furlanetto S. R., 2005, submitted to *ApJ* (astro-ph/0512263)
 Mellema G., Iliev I. T., Alvarez M. A., Shapiro P. R., 2006, *New Astronomy*, 11, 374
 Merz H., Pen U.-L., Trac H., 2005, *New Astronomy*, 10, 393
 Morales M. F., Hewitt J., 2004, *ApJ*, 615, 7
 Page L., Hinshaw G., Komatsu E., Nolta M. R., Spergel D. N., Bennett C. L., Barnes C., Bean R., Doré O., Halpern M. e. a., 2006, *ApJ*, submitted
 Purcell E. M., Field G. B., 1956, *ApJ*, 124, 542
 Shapiro P. R., Ahn K., Alvarez M. A., Iliev I. T., Martel H., Ryu D., 2005, submitted to *ApJ* (astro-ph/0512516)
 Shapiro P. R., Iliev I. T., Raga A. C., 2004, *MNRAS*, 348, 753
 Shaver P. A., Windhorst R. A., Madau P., de Bruyn A. G., 1999, *A&A*, 345, 380
 Spergel D. N., Verde L., Peiris H. V., Komatsu E., Nolta M. R., Bennett C. L., Halpern M., Hinshaw G., Jarosik N., Kogut A., Limon M., Meyer S. S., Page L., Tucker G. S., Weiland J. L., Wollack E., Wright E. L., 2003, *ApJS*, 148, 175
 Valdes M., Ciardi B., Ferrara A., Johnston-Hollitt M., Rottgering H., 2006, submitted to *MNRAS* (astro-ph/0602560)
 Wouthuysen S. A., 1952, *AJ*, 57, 31
 Zaldarriaga M., Furlanetto S. R., Hernquist L., 2004, *ApJ*, 608, 622
 Zygelman B., 2005, *ApJ*, 622, 1356